

Differential phase contrast from electrons that cause inner shell ionization

Michael Deimetry^a, Timothy C. Petersen^b, Hamish G. Brown^c, Matthew Weyland^b, Scott D. Findlay^{a,*}

^a*School of Physics and Astronomy, Monash University, Clayton, Victoria, 3800, Australia*

^b*Monash Centre for Electron Microscopy, Monash University, Clayton, Victoria, 3800, Australia*

^c*Ian Holmes Imaging Center, University of Melbourne, Parkville, Victoria, 3052, Australia*

Abstract

Differential Phase Contrast (DPC) imaging, in which deviations in the bright field beam are in proportion to the electric field, has been extensively studied in the context of pure elastic scattering. Here we discuss differential phase contrast formed from core-loss scattered electrons, i.e. those that have caused inner shell ionization of atoms in the specimen, using a transition potential approach for which we study the convergence properties. In the phase object approximation, we show formally that this is mainly a result of preservation of elastic contrast. Through simulation we demonstrate that whether the inelastic DPC images show element selective contrast depends on the spatial range of the ionization interaction, and specifically that when the energy loss is low the delocalisation can lead to contributions to the contrast from atoms other than that ionized. We further show that inelastic DPC images remain robustly interpretable to larger thicknesses than is the case for elastic DPC images, owing to the incoherence of the inelastic wavefields, though subtleties due to channelling remain.

Keywords: Differential phase contrast, 4D STEM, inner shell ionization

1. Introduction

Fast readout electron pixel detectors are facilitating a range of momentum-resolved imaging modes now broadly referred to as four-dimensional scanning transmission electron microscopy¹ (4D STEM) [2], in which two-dimensional diffraction patterns are recorded at each position as a converged electron probe is raster scanned across the surface of a specimen. At nanometer resolution, this includes orientation mapping [3, 4], strain measurement via nanobeam electron diffraction [5, 6], and electromagnetic field mapping via differential phase contrast (DPC, also called centre-of-mass or first moment imaging) [7, 8, 9]. At atomic resolution, this includes atomic-resolution DPC [10, 11] and various forms of electron ptychography [12, 13, 14]. These techniques

*Corresponding author

Email address: `scott.findlay@monash.edu` (Scott D. Findlay)

¹Not to be confused with STEM electron energy loss spectroscopy (EELS) tomography which is also referred to as 4D STEM EELS [1].

are predicated on the elastic scattering behaviour of electrons. Inelastic scattering is a confounding factor for these techniques, that can be mitigated if the 4D STEM data are zero-loss energy filtered [15]. However, STEM with an energy filter before a fast-readout pixel detector, as depicted in Fig. 1(a), allows for additional imaging possibilities.

Simultaneous momentum and energy resolution has a long history in conventional TEM [16]. In STEM, Midgley et al. [17] showed a core-loss-filtered (i.e. from probe electrons that caused inner shell ionization events) convergent-beam electron diffraction pattern containing chemically-sensitive features in 1995. More recently, experimental realisation of simultaneous momentum and energy resolution in STEM by using an energy filter in front of a fast readout pixel detector has mainly focused on so-called ω - q imaging, resolving one direction of momentum transfer and energy loss to probe dispersion relations in plasmon and phonon scattering [18, 19]. Haas and Koch [20] used ω - q imaging with multiple slit orientations to synthesise core-loss-filtered DPC images of monolayer hexagonal boron nitride (hBN), showing atomic-resolution contrast qualitatively similar to that in zero-loss-filtered DPC images. While frameworks in which to simulate core-loss-filtered diffraction patterns are well established [21, 22, 23] – notably, Müller-Caspary et al. [24] showed that simulated diffraction patterns in core-loss-filtered 4D STEM can contain rich structure that varies with probe position – there has been little exploration of how core-loss-filtered diffraction patterns might be interpreted.

This paper explores the imaging formation dynamics of DPC imaging from core-loss-filtered 4D STEM, describing core-loss scattering via the transition potential formulation [21, 23, 25, 26]. Our exploration is centred around two key results. The first is the experimental finding of Haas and Koch [20] that the zero-loss-filtered and core-loss-filtered DPC images have qualitatively similar appearance, as reproduced in the simulated DPC images for hBN in Fig. 1(b) and (c) respectively. In particular, the nitrogen atoms are clearly visible in the core-loss-filtered DPC image for the boron K-edge, and so, in this case, core-loss-filtered DPC imaging is not providing element-specific contrast. The second, demonstrated in the simulated DPC images for 200 Å thick SrTiO₃ in Fig. 1(d) and (e), is that the image contrast in core-loss-filtered DPC imaging (Fig. 1(e)) is more robust with respect to thickness (and defocus) than that in zero-loss-filtered DPC imaging (Fig. 1(d)).

A brief note on terminology is warranted. While there is a close analogy between energy-filtered transmission electron microscopy (EFTEM) and energy-filtered 4D STEM, as an acronym ‘EFSTEM’ is already used in different contexts [27]. For specificity, we will therefore refer to energy-filtered DPC, abbreviated to EFDPC, which unless otherwise specified should in this work be understood to mean core-loss filtering.

2. Transition potential formulation of core-loss scattering

To simulate core-loss-filtered 4D STEM data, we follow the approach of Coene and Van Dyck [26], further developed for core-loss transitions by Dwyer [21]. The basic concept is sketched in Fig. 2 for a single layer of atoms. The inelastically-scattered wavefield ψ_f that results when an incident elastic wave ψ_i excites an atom from its initial state i to some final state f is given by [21, 25, 26]

$$\psi_f(\mathbf{r}_\perp) = -i\sigma H_{fi}(\mathbf{r}_\perp)\psi_i(\mathbf{r}_\perp) , \quad (1)$$

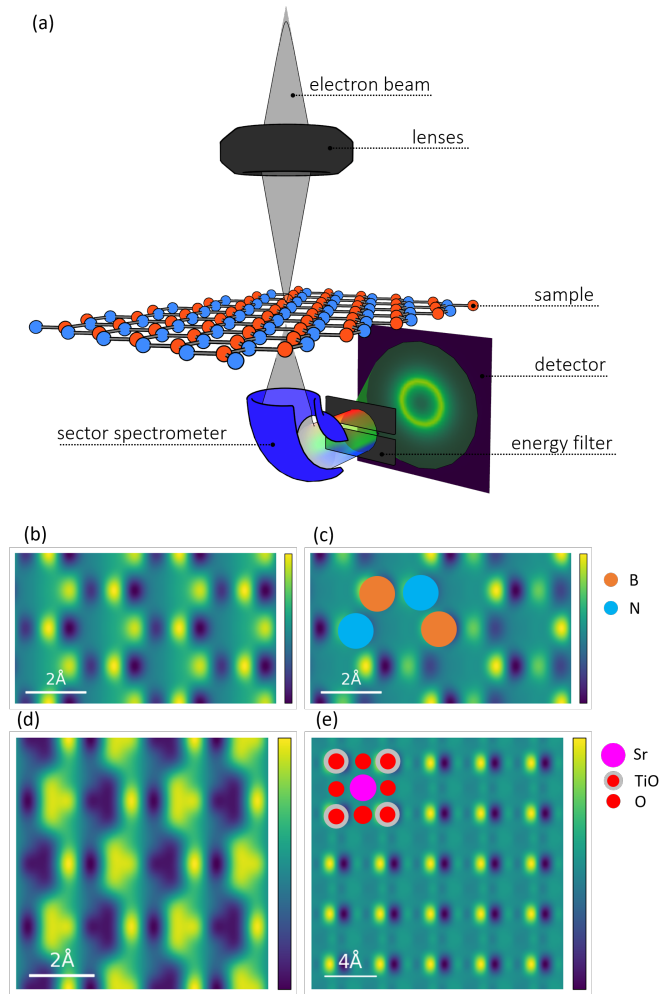


Figure 1: (a) Simplified schematic of the energy-filtered 4D STEM setup. An electron probe is raster scanned across a monolayer of hBN. The electrons pass through a spectrometer with a slit chosen to only let through electrons with kinetic energies in a desired energy range. (b) Elastic and (c) inelastic (with energy filter 50 eV above the boron K-shell edge) simulated DPC images for monolayer hBN. The nitrogen columns are more pronounced in the elastic image, but still clearly visible in the inelastic image from the boron K-shell. (d) Elastic and (e) inelastic (with energy filter 50 eV above the Ti L₁-shell) DPC images for 200 Å thick SrTiO₃. Whereas at this thickness it is difficult to interpret the structure clearly from the elastic image, the inelastic image is more robustly interpretable, with the Ti column locations showing clear differential phase contrast. These simulations assume 300 keV beam electrons and a 15.7 mrad probe-forming convergence semiangle.

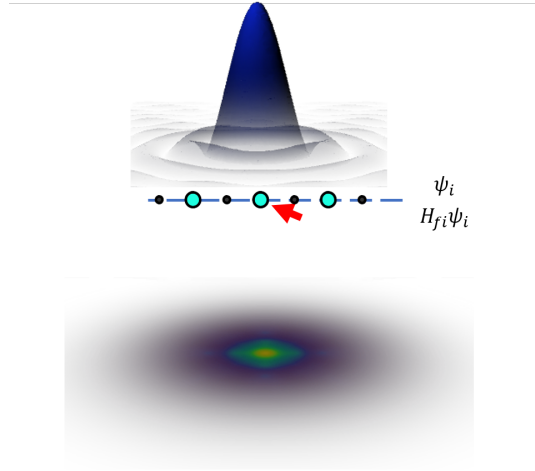


Figure 2: Schematic of the inelastic scattering process in a monolayer of atoms. The incident wavefield ψ_i produces an inelastic wave with probability governed by the transition potential H_{fi} . This procedure is repeated for each final state of each atom of the ionized species, and the resultant diffraction patterns are summed incoherently.

where \mathbf{r}_\perp are the real-space coordinates transverse to the optic axis, $\sigma = \gamma m_0 \lambda / 2\pi \hbar^2$ (in which γ is the Lorentz factor, m_0 is the electron rest mass, λ is the relativistically-corrected de-Broglie wavelength and \hbar is the reduced Planck's constant), and $H_{fi}(\mathbf{r}_\perp)$ is a (projected) transition potential². Since for the single plane of atoms depicted in Fig. 2 the wavefield $\psi_f(\mathbf{r}_\perp)$ is at the exit surface of the sample, its contribution to the diffraction pattern is given by the intensity of its Fourier transform. The principles of quantum mechanics oblige us to (incoherently) sum all contributions from sample final states that are not directly observed but which are consistent with what is measured. Thus the core-loss-filtered diffraction intensity may be written

$$\mathcal{I}(\mathbf{k}_\perp) = \sum_f |\mathcal{F}\{\psi_f\}(\mathbf{k}_\perp)|^2, \quad (2)$$

where the sum over f includes all inner shell ionization final states consistent with the selected energy loss (in practice, rather an energy loss range), \mathcal{F} denotes Fourier transform, and \mathbf{k}_\perp denotes the diffraction plane coordinate.

Following Dwyer [21] in assuming a central field, one-electron wavefunction model for the atomic electron being ejected through the ionization event, we label the initial states via the quantum numbers n (principal quantum number), ℓ (orbital quantum number) and m (magnetic quantum number), and the final states via the quantum numbers ε (being the kinetic energy of the ejected electron, equal to the energy loss above the atom's ionization threshold), ℓ' and m'

²In the literature $H_{fi}(\mathbf{r}_\perp)$ is also referred to as a projected matrix element, Møller potential or simply a matrix element. The choice of units also varies, with other choices leading to a prefactor that differs accordingly from the σ of Eq. (1).

(the orbital and magnetic quantum numbers, respectively). Throughout this paper, we adopt the convention of denoting continuum orbital and magnetic quantum numbers using primed variables. The three-dimensional transition potentials in reciprocal space are given by [21, 25]

$$H_{n\ell m \rightarrow \varepsilon \ell' m'}(\mathbf{k}) = \frac{q_e^2}{4\pi^2 \varepsilon_0 k^2} \int d\mathbf{r} a_{n\ell m}(\mathbf{r}) a_{\varepsilon \ell' m'}^*(\mathbf{r}) e^{-i2\pi \mathbf{k} \cdot \mathbf{r}}, \quad (3)$$

where q_e is the elementary charge and ε_0 is the permittivity of free space. Equation (3) corresponds to the coupling of the bound state $a_{n\ell m}(\mathbf{r})$ and the continuum state $a_{\varepsilon \ell' m'}(\mathbf{r})$ of the atomic electron ejected during the ionization event.³ The projected transition potential appearing in Eq. (1) is then obtained by [21, 25]

$$H_{f_i}(\mathbf{r}_\perp) = \int_{-\infty}^{\infty} dz' e^{-i2\pi(k_f - k_i)z'} H_{f_i}(\mathbf{r}_\perp, z') \quad (4)$$

$$= \int d\mathbf{k}_\perp H_{f_i}(\mathbf{k}_\perp, k_f - k_i) e^{i2\pi \mathbf{k}_\perp \cdot \mathbf{r}_\perp}, \quad (5)$$

where the second equality follows by the Fourier projection theorem, and $k_f - k_i$ is related to the energy loss of the probe electron. We will refer to H_{f_i} simply as a transition potential, with the argument implicitly denoting whether the potential is projected or otherwise.

Writing the bound and continuum states explicitly as a product of angular and radial terms⁴, $a_{n\ell m}(\mathbf{r}) = Y_\ell^m(\hat{\mathbf{r}})P_{n\ell}(r)/r$ and $a_{\varepsilon \ell' m'}(\mathbf{r}) = Y_{\ell'}^{m'}(\hat{\mathbf{r}})P_{\varepsilon \ell'}(r)/r$, Eq. (3) can be simplified to

$$H_{n\ell m \rightarrow \varepsilon \ell' m'}(\mathbf{k}) = \frac{q_e^2}{4\pi^2 \varepsilon_0 k^2} \sum_{\ell''=|\ell'-\ell|}^{\ell'+\ell} (-i)^{\ell''} Y_{\ell''}^{m-m'}(\hat{\mathbf{k}}) \langle \ell' m' | \overline{\ell'' (m-m')} | \ell m \rangle R_{\nu', \ell'', \ell}(k), \quad (6)$$

where the Gaunt coefficient

$$\begin{aligned} \langle \ell' m' | \overline{\ell'' m''} | \ell m \rangle &= \int d\hat{\mathbf{q}} Y_{\ell'}^{m'*}(\hat{\mathbf{q}}) Y_{\ell''}^{m''*}(\hat{\mathbf{q}}) Y_\ell^m(\hat{\mathbf{q}}) \\ &= (-1)^{m'+m''} \sqrt{\frac{(2\ell'+1)(2\ell''+1)(2\ell+1)}{4\pi}} \begin{pmatrix} \ell' & \ell'' & \ell \\ 0 & 0 & 0 \end{pmatrix} \begin{pmatrix} \ell' & \ell'' & \ell \\ -m' & -m'' & m \end{pmatrix} \end{aligned} \quad (7)$$

(in which the array-like objects are Wigner 3-j symbols), and

$$R_{\nu', \ell'', \ell}(k) = \int_0^\infty dr P_{\varepsilon \ell'}(r) j_{\ell''}(kr) P_{n\ell}(r) = \sqrt{\frac{\pi}{2k}} \mathbb{H}\mathbb{T}_{\ell''+1/2} \left\{ \frac{P_{\varepsilon \ell'}(r) P_{n\ell}(r)}{r^{3/2}} \right\} (k) \quad (8)$$

(in which $j_{\ell''}$ are spherical Bessel functions of order ℓ'' of the first kind) can be computed efficiently using the fast Hankel transform⁵. Calculations in this paper are based on these ideas as

³We will not consider bound-bound transitions, though they can be described by a similar formalism [28].

⁴Following Ref. [29], we use relativistic Hartree-Fock wave functions for the bound states and Hartree-Slater wave functions for the continuum states.

⁵The Hankel transform is defined as

$$\mathbb{H}\mathbb{T}_\mu\{f\}(k) = \int_0^\infty dr f(r) J_\mu(kr) r,$$

where J_μ is a μ^{th} order Bessel function of the first kind.

implemented in `py_multislice` [30].

Figure 3 shows various titanium $L_{2,3}$ -shell excitation probabilities. The greatest amplitude is near the atom, implying beam electrons closest to the titanium atom are more likely to cause ionization events. The vortex phase structure occurs because, despite the sum over ℓ'' in Eq. (6), all the azimuthal dependence is contained in a phase factor of the form $e^{i(m-m')\phi_k}$. The so-called winding number of the vortex is given by $m - m'$, where positive values imply increasing phase in the clockwise direction. The transitions are related by the magnetic quantum numbers through the relationship

$$H_{\ell(-m)\rightarrow\ell'(-m')}^*(\mathbf{r}_\perp) = (-1)^{\ell'+\ell} H_{\ell m\rightarrow\ell' m'}(\mathbf{r}_\perp) \quad (9)$$

which is seen in Fig. 3, where the tiles (m, m') and $(-m, -m')$, located in the diametrically opposed position about the $(m = 0, m' = 0)$ tile, have opposite winding numbers due to the complex conjugation in Eq. (9).

The transition potentials in each tile in Fig. 3 are normalised to a common maximum magnitude to make the phase structure clear. However, this obscures that the magnitudes vary significantly. In particular, they tend to decrease with increasing ℓ' . Transitions which are unlikely to be realized can be neglected with little consequence on the accuracy of the calculation. Indeed, simulation relies on being able to reduce the in-principle infinite number of final states to sum over in Eq. (2) (ℓ' being any non-negative integer) to a limited number that capture the majority of the inelastic scattering probability. The probability of inelastic scattering into different final states f is, for the same incident wavefield, bounded⁶ by the integrated intensity in H_{fi} . We therefore consider the rate of convergence of the following sequence in ℓ' :

$$T_{\ell'}(n\ell, \varepsilon) = \sum_{m, m'} \int d\mathbf{r}_\perp |H_{n\ell m\rightarrow\varepsilon\ell' m'}(\mathbf{r}_\perp)|^2. \quad (10)$$

A remarkable pattern emerges when the sequence (normalised by the $\ell' = 0$ term) is plotted on a log scale as illustrated in Fig. 4. Beginning from $\ell' = 2$ for K-shell and $\ell' = 4$ for L_1 -shell, the terms of the sequence fall off exponentially (linear behaviour with the vertical scale plotted logarithmically). This fall-off varies depending on several experimental parameters: the atomic number Z is most significant, followed by the energy loss above ionization threshold ε . The dependence on accelerating voltage is not shown because it is very weak indeed.

As derived in the supplementary material, an approximate analytic expression for the fall-off observed for the K-shell is given by

$$\log_{10} \left[\frac{T_{\ell'}(n\ell, \varepsilon)}{T_0(n\ell, \varepsilon)} \right] \sim 2\ell' \left[\log_{10} e + \frac{1}{2} \log_{10} |\varepsilon/R_d - Z^{2/7}| - \log_{10}(\zeta) \right] + \text{terms weakly depending on } \ell', \quad (11)$$

⁶This follows by applying the triangle inequality to the integrated intensity on both sides of Eq. (1), an idea developed further in the Supplementary Material.

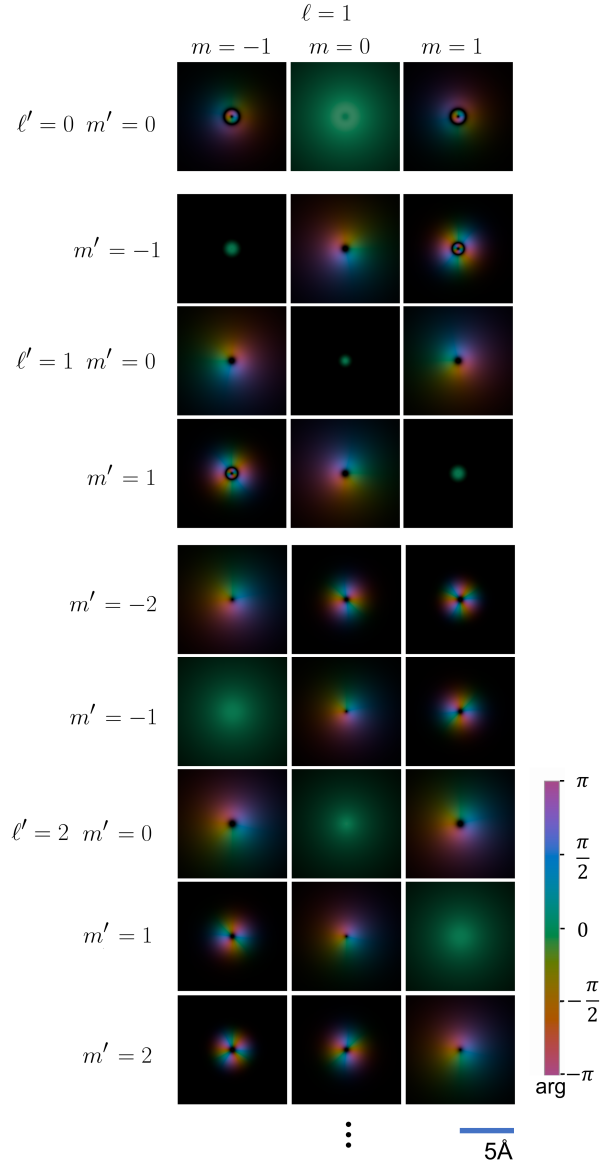


Figure 3: L_{2,3}-shell titanium transition probabilities, $H_{nlm \rightarrow \ell' m'}$, for beam energy 80keV and $\varepsilon = 10\text{eV}$. The magnitude, depicted as brightness, shows that beam electrons near the atom are most likely to cause ionization events. The phase, depicted modulo 2π by colour, has a vortex structure with the winding number given by $m - m'$.

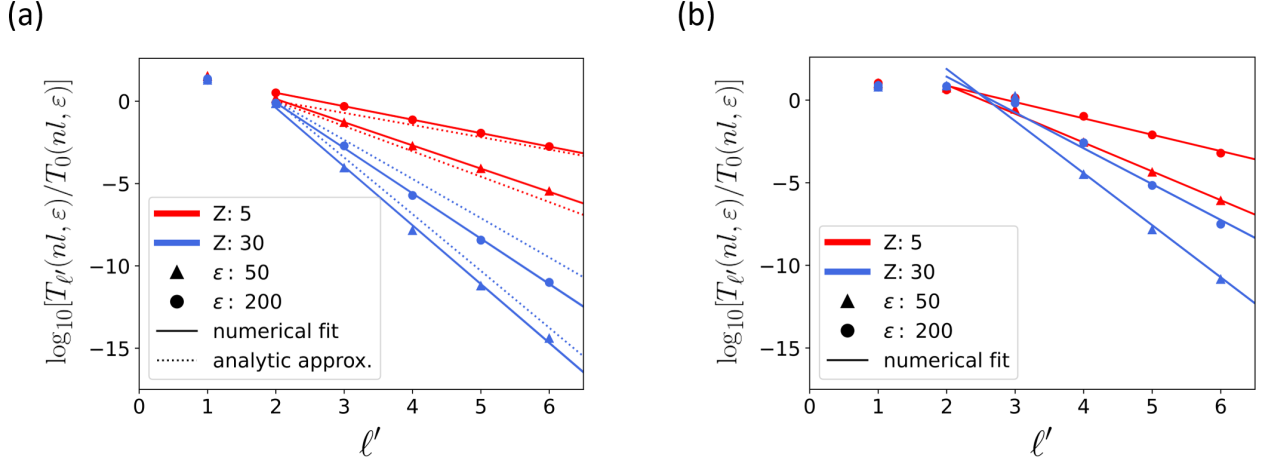


Figure 4: Sequence in Eq. (10) (normalised by the $\ell' = 0$ term) plotted for boron and zinc for ionization energies 50 eV and 200 eV above the (a) K- and (b) L_1 - shell edge. Solid lines are a guide to the eye, emphasising the linear trend. Dotted lines show the prediction of the approximate analytic expression, Eq. (11), for K-shell ionization.

where $\zeta \approx Z$ and $R_d = 13.6$ eV. A correction factor of $Z^{2/7}$ is included based on empirical considerations. This approximation is plotted in Fig. 4(a) by dotted lines (though not Fig. 4(b) since the analytic approximations we have used do not hold for L_1 edge), and seen to be in good qualitative agreement with the more detailed calculation. Equation (11) shows specifically that Z and ε have approximately equal effects on the fall-off, albeit in opposite directions. For instance, doubling Z and halving ε leaves the fall-off approximately unchanged.

3. Case study – monolayer materials

To clarify the similarities and differences, let us first re-derive the elastic DPC expression before proceeding to EFDPC. For an elastic wavefield Ψ , the first moment of the diffraction intensity is given by

$$\mathbf{C} = \int \mathbf{k}_\perp |\Psi(\mathbf{k}_\perp)|^2 d\mathbf{k}_\perp = \frac{i}{2\pi} \int \psi(\mathbf{r}_\perp) [\nabla_{\mathbf{r}_\perp} \psi^*(\mathbf{r}_\perp)] d\mathbf{r}_\perp, \quad (12)$$

where $\psi(\mathbf{r}_\perp)$ is the exit surface wave function with Fourier transform $\mathcal{F}\{\psi\} = \Psi(\mathbf{k}_\perp)$. The second equality follows by the Fourier derivative theorem. Within the phase object approximation, the exit surface wave function resulting from elastic scattering takes the form

$$\psi(\mathbf{r}_\perp) = e^{i\phi(\mathbf{r}_\perp)} \psi_0(\mathbf{r}_\perp - \mathbf{R}), \quad (13)$$

where the transmission function phase $\phi(\mathbf{r}_\perp) = \sigma V(\mathbf{r}_\perp)$ (i.e. is proportional to the specimen projected potential $V(\mathbf{r}_\perp)$), ψ_0 is the entrance surface wave field, and \mathbf{R} is the probe position on

the specimen surface. Substituting Eq. (13) into Eq. (12) yields

$$\mathbf{C}(\mathbf{R}) = \frac{1}{2\pi} \int d\mathbf{r}_\perp [\nabla_{\mathbf{r}_\perp} \phi(\mathbf{r}_\perp)] |\psi_0(\mathbf{r}_\perp - \mathbf{R})|^2 + \frac{i}{2\pi} \int d\mathbf{r}_\perp \psi_0(\mathbf{r}_\perp - \mathbf{R}) \nabla_{\mathbf{r}_\perp} \psi_0^*(\mathbf{r}_\perp - \mathbf{R}) . \quad (14)$$

When the probe-forming aperture is symmetric, the second term in Eq. (14) is identically zero, and thus [31]

$$\mathbf{C}(\mathbf{R}) = \frac{1}{2\pi} |\psi_0(\mathbf{R})|^2 \star \nabla \phi(\mathbf{R}) , \quad (15)$$

where \star denotes cross correlation.

In the inelastic regime, for a single transition the exit surface wavefield within the multiplicative-object approximation is given by both the transition of an elastic to an inelastic wavefield as per Eq. (1) and transmission through the specimen as per Eq. (13):

$$\psi(\mathbf{r}_\perp) = -i\sigma H_{fi}(\mathbf{r}_\perp) e^{i\phi(\mathbf{r}_\perp)} \psi_0(\mathbf{r}_\perp - \mathbf{R}) . \quad (16)$$

To describe the inelastic case for inner shell ionization, not only must we sum over all final states as per Eq. (2) but it is also appropriate to sum over the different possible initial states which produce the same energy loss. Specifically, neglecting fine structure, this means summing over initial magnetic quantum number m and spin states s . The appropriate generalisation of Eq. (2) is then

$$\mathcal{I}(\mathbf{k}_\perp) = \sum_{\substack{\text{atoms} \\ m, s, \ell', m'}} |\Psi_{nlm \rightarrow \varepsilon \ell' m'}(\mathbf{k}_\perp)|^2 , \quad (17)$$

where n and ℓ are fixed by the EELS edge chosen and ε is fixed by the excitation energy above threshold. We will use the shorthand notation $\sum_{a, fi}$ for this summation in subsequent equations, with a distinguished from f to emphasise that we must sum over multiple atomic sites as well as final states for each atom.

Replacing the coherent intensity in Eq. (12) with the incoherent intensity in Eq. (17) using the wavefields of Eq. (16) yields

$$\begin{aligned} \mathbf{C}(\mathbf{R}) = & \frac{\sigma^2}{2\pi} |\psi_0(\mathbf{R})|^2 \star \left[\sum_{a, fi} |H_{fi}(\mathbf{R})|^2 \nabla \phi(\mathbf{R}) \right] \\ & + \frac{i\sigma^2}{2\pi} \sum_{a, fi} \int H_{fi}(\mathbf{r}_\perp) \psi_0(\mathbf{r}_\perp - \mathbf{R}) \nabla_{\mathbf{r}_\perp} (H_{fi}(\mathbf{r}_\perp) \psi_0(\mathbf{r}_\perp - \mathbf{R}))^* d\mathbf{r}_\perp . \end{aligned} \quad (18)$$

Akin to elastic DPC, it can be shown (see appendix Appendix A) that the second term in Eq. (18) is identically zero for a rotationally-symmetric, aberration-free probe when initial and final states (specifically, m and m') are summed over. Even when the probe contains aberrations which break the rotational symmetry, the second term in Eq. (18) is at least an order of magnitude smaller than the first term. We thus neglect the second term to yield

$$\mathbf{C}(\mathbf{R}) = \frac{\sigma^2}{2\pi} |\psi_0(\mathbf{R})|^2 \star \left[\sum_{a, fi} |H_{fi}(\mathbf{R})|^2 \nabla \phi(\mathbf{R}) \right] . \quad (19)$$

This inelastic DPC expression is very similar in form to the elastic CoM expression in Eq. (15), save now that the phase gradient is modulated by the inelastic transition probability. In particular, the contrast does not arise from the inelastic scattering (interpreted to be the $H_{fi}(\mathbf{R})$ transition potential) but rather from the elastic scattering (interpreted to be $\phi(\mathbf{R})$, the phase of the elastic scattering transmission function). The result can thus be considered an example of preservation of elastic contrast [32, 33], where contrast deriving from the elastic scattering is retained in the inelastic signal.

Strictly speaking, Eq. (19) means the DPC image is no longer an exact gradient. However, if the inelastic transition probability is approximately constant in the vicinity of the atom sites then

$$\sum_{a,fi} |H_{fi}|^2 \nabla \phi \approx \nabla \left(\sum_{a,fi} |H_{fi}|^2 \phi \right). \quad (20)$$

When this approximation holds, the EFDPC signals can be integrated in the same way as DPC signals to give an integrated DPC (iDPC) signal [34]:

$$\left(\phi \sum_{a,fi} |H_{fi}|^2 \right) (\mathbf{R}) \approx \mathcal{F}^{-1} \left\{ \frac{\mathcal{F}\{C_x\}(\mathbf{k}_\perp) + i\mathcal{F}\{C_y\}(\mathbf{k}_\perp)}{2\pi i(k_x + ik_y) \mathcal{F}\{|\psi_0|^2\}(\mathbf{k}_\perp)} \right\} (\mathbf{R}), \quad (21)$$

where $\mathbf{k}_\perp = (k_x, k_y)$ are taken to be Fourier space coordinates and C_x and C_y are the components of Eq. (19).

The interpretation of Eqs. (19) and (21) depends on the spatial extent of the transition probabilities $|H_{fi}|^2$. If they are so delocalised that $\sum_{a,fi} |H_{fi}|^2$ would be approximately constant throughout the material then the inelastic DPC signal would be proportional to the elastic DPC signal, with contrast from all atoms visible. (This is consistent with the results of Beyer et al. [35] for plasmon-loss-filtered, atomic-resolution DPC.) If they are sufficiently localised as to become negligible over the interatomic distance in the direction transverse to the beam axis then only the columns containing the ionized elements will appear in the image, producing element selective contrast. If they are between these limits, being non-zero but reduced in magnitude at adjacent atomic sites, then those sites will appear in the EFDPC image with reduced contrast (relative to the elastic case).

The spatial extent of the transition probabilities $|H_{fi}|^2$ depends on accelerating voltage of the beam, the ionization edge (i.e. the atomic species and the initial state), and the energy loss above the atom's ionization threshold, ε . This is explored in the EFDPC image tableaus over ε and atomic number Z in Fig. 5(a) and (b). In the case $Z=5$ the structure is monolayer hBN; for other Z we assume a fictitious structure in which the boron atoms are replaced by atoms of that atomic number. In Fig. 5(a), the K-shell ionization of that atom is assumed; in Fig. 5(b), L₁-shell ionization is assumed. The transition potentials become more localized with increasing atomic number and/or energy above threshold, and consequently the contrast at the nitrogen atom sites, indicated by arrows, become fainter.

Hence, for element-selective contrast corresponding to a low atomic number ($\lesssim 8$) the energy window needs to be several tens of electron volts above the ionization edge. For larger atomic numbers, the energy window can be moved closer to the ionization edge. Since fewer inelastic events

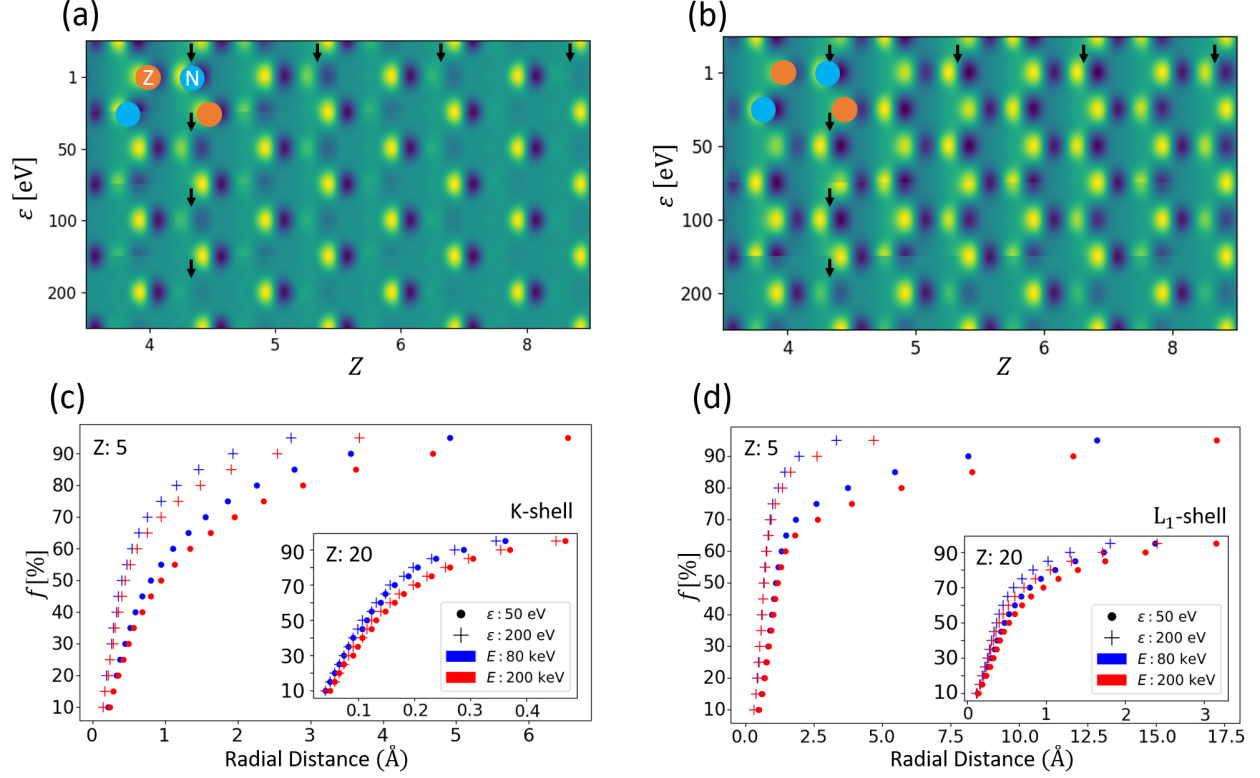


Figure 5: (a) K-shell and (b) L₁-shell EFDPC tableaux assuming a hBN-like structure and varying Z , the atomic number of the atoms at what in hBN would be the boron site, and ϵ . These simulations assume 300 keV beam electrons and a 15.7 mrad probe-forming convergence semiangle. The arrows indicate nitrogen sites where there is a gradual reduction in contrast with increasing Z (of the atom being ionized) and/or energy above threshold. To convey in more detail the spatial localization of the transition potentials, we show what percentage of the transition probability (integrated mod-square of the transition potential) is contained within a given radius (see Eq. (22)) for (c) K-shell (d) L₁-shell for all possible combinations of $Z : 5, 20$, $\epsilon : 50, 200$ eV and beam energy $E : 80, 200$ keV up to $\ell' = 5$ inclusive.

will occur further from the ionization edge, lower atomic numbers present the greatest challenge experimentally. The experimental images of Haas and Koch [20] of boron K-shell ionization do not show boron-selective contrast, instead having contrast evident at the nitrogen sites too. This is expected since for element-selective contrast for boron the energy window need to be placed around 50 eV above the K-edge. However, since this distance from the edge will yield much lower signal-to-noise, the energy filter for that experiment was likely positioned a few electron volts beyond the boron K-edge.

We can quantify the spatial localization of the transition potentials by considering the radial distance from the atom within which some fraction of all transitions are expected to occur. That

is, we solve

$$\frac{\int_0^r \int_0^{2\pi} dr r d\theta \sum_{f_i} |H_{f_i}(r, \theta)|^2}{\int_0^\infty \int_0^{2\pi} dr r d\theta \sum_{f_i} |H_{f_i}(r, \theta)|^2} = f \quad (22)$$

for r for various $0 < f < 1$. Since the final CoM image will contain contributions from all allowed intermediate states, Eq. (22) does not distinguish the individual transition contributions to the overall fraction of all expected transitions, hence the summation over final states. Figure 5(c) and (d) contain the solution of Eq. (22) for all combinations of the accelerating voltage $E : 80, 200$ keV, the ionization energy above threshold $\varepsilon : 50, 200$ eV, the atomic number $Z : 5, 20$ and the K, L_1 shells. The summation in Eq. (22) is truncated at $\ell' = 5$ inclusive since, as implied by Fig. 4, the remaining transitions are heavily suppressed. For small atomic numbers both beam energy and ε are significant in the potential's localization albeit ε is dominant. However, this dependence gradually flips for larger atomic numbers. The same is true, but more pronounced, for higher shells.

4. Case study – thick specimen

The previous section showed that if the transition potentials were sufficiently localised then EFDPC images showed differential phase contrast arising from the gradient of the elastic potential with element-selectivity resulting from the inelastic scattering event selected. This followed from the phase object approximation of Eq. (16). At atomic resolution, the phase object approximation has been shown to break down for thicknesses beyond a few nanometers for elastic differential phase contrast [36, 37]. In this section we explore the interpretability of EFDPC images from thicker samples as the phase object approximation breaks down and dynamical diffraction becomes significant.

To simulate core-loss-filtered diffraction patterns for thick samples, we use the efficient scattering-matrix-based approach of Brown et al. [23], building on the transition potential relation in Eq. (1) by incorporating the elastic scattering of the wavefield in the sample before and after each inelastic transition. Consider a particular transition H_{f_i} of the particular atom indicated by the arrow in Fig. 6. The elastic scattering of the entrance surface wavefield ψ_0 to the plane containing the particular atom in question is denoted here by the scattering matrix operator \mathcal{S}_1 , and subsequent elastic scattering of the inelastic wavefield to the exit surface is denoted by the scattering matrix operator \mathcal{S}_2 . Thus Eq. (1) generalises to a thick sample as

$$\psi_f(\mathbf{r}_\perp) = -i\sigma\mathcal{S}_2H_{f_i}(\mathbf{r}_\perp)\mathcal{S}_1\psi_i(\mathbf{r}_\perp), \quad (23)$$

where the scattering matrix operators are understood to effect elastic scattering through the crystal. As before, the total inelastic diffraction pattern is the incoherent sum of the contributions, i.e. the intensity of the Fourier transform of Eq. (23), for each final state (or at least enough to obtain a converged calculation, as per the discussion of Fig. 4), repeated for each atom of the same species. We evaluate the scattering matrix operator via absorptive multislice calculations. As shown by Brown et al. [23], the advantage of the scattering matrix approach is that for each depth the scattering matrix can be evaluated just once but then applied to all the inelastic transitions that

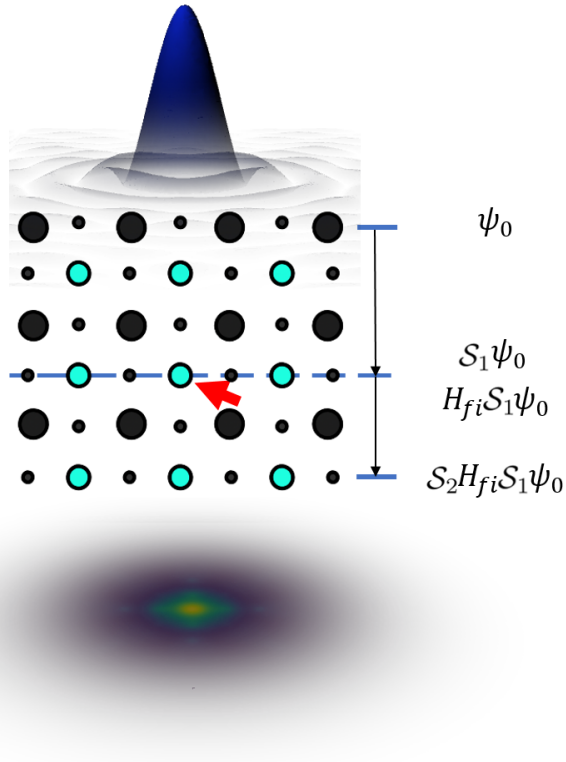


Figure 6: Schematic of the inelastic scattering process in a thick specimen of condensed matter. The incident wavefield ψ_0 is elastically propagated using the scattering matrix \mathcal{S}_1 to the depth of the atom being ionized, produces an inelastic wave with probability governed by the transition potential H_{fi} , and is then elastically propagated using the scattering matrix \mathcal{S}_2 to the exit surface. This procedure is repeated for each final state of each atom of the ionized species, and the resultant diffraction patterns are summed incoherently.

take place at that depth. Note that we only consider single inelastic scattering, since the probability of ionization is sufficiently small that the probability of the same beam electron ionizing multiple atoms is negligible for typical sample thickness in atomic-resolution STEM.

Taking the prototypical example of SrTiO₃, following Ref. [36] we can explore the breakdown of the phase object approximation using a thickness-defocus tableau, a mosaic of DPC images across various thicknesses and probe defocus values. Because simulating for a range of thickness and defocus values is time-consuming, in the calculations that follow we have restricted the extent of the detector to 35 mrad, which in the methodology of Ref. [23] limits the size of the \mathcal{S}_2 operator and thereby the computational complexity. For core-loss transitions, the contributions for higher scattering angles are more significant than in the elastic case [24] and so limiting the detector extent results in an underestimate of the inelastic DPC contrast. However, the qualitative appearance of the images is not appreciably affected, and the detector extent would anyway be limited in practice. We also limit the final states to $\ell \leq 2$, since, as per Fig. 4, the terms $\ell = 3$ are small enough to be neglected.

To make evident when the phase object approximation breaks down quantitatively, we normalise each DPC image in the tableau according to the sample thickness. Equation (15) shows that the elastic DPC image will increase linearly with thickness (assuming a specimen periodic along the beam direction) since the phase of the transmission function ϕ , which is proportional to the projected potential, is linearly proportional to thickness. Hence, normalising the elastic DPC images by the sample thickness will lead to the contrast within each unit cell being independent of thickness within the phase object approximation's domain of applicability. This is seen in the elastic DPC tableau in the left panel in Fig. 7: up to a thickness of roughly 35 Å, the contrast is largely independent of thickness. Beyond that thickness, the decrease in contrast is evidence of the quantitative breakdown of the phase object approximation. For still larger thicknesses, the pattern starts to change as the breakdown of the phase object approximation impacts the interpretability of the images. For the present parameters the depth of focus is around 130 Å and so the defocus dependence in the figure is weak over the range shown, though the finding that in the phase object approximation the contrast is maximised when the probe is focused on the specimen midplane [36] is perceptible in the images at larger thicknesses being more interpretable for greater defocus into the sample.

In the inelastic case, Eq. (19), in addition to the linear dependence of ϕ on sample thickness, the incoherent summation of contributions from the atoms along the column is also linear in thickness. Hence, normalising the EFDPC images by the square of the sample thickness will lead to the contrast within each unit cell being independent of thickness within the phase object approximation's domain of applicability. This is seen in the EFDPC tableau for the Ti L₁-edge in the right panel in Fig. 7. The quantitative domain of validity of the phase object approximation is seen to be consistent with the elastic case, with very similar contrast seen for thicknesses below 35 Å but a decrease in contrast at larger thicknesses. However, excepting for large defocus in the thinnest sample, the pattern in the EFDPC image persists to larger thicknesses than in the elastic case.

To show that this qualitative robustness persists to still larger thicknesses, Fig. 8 shows thickness-defocus tableaus for (a) elastic DPC, and for EFDPC of (b) the O-K edge, and (c) Ti L₁-edge. These extended tableaus are not thickness-normalised and more clearly show that

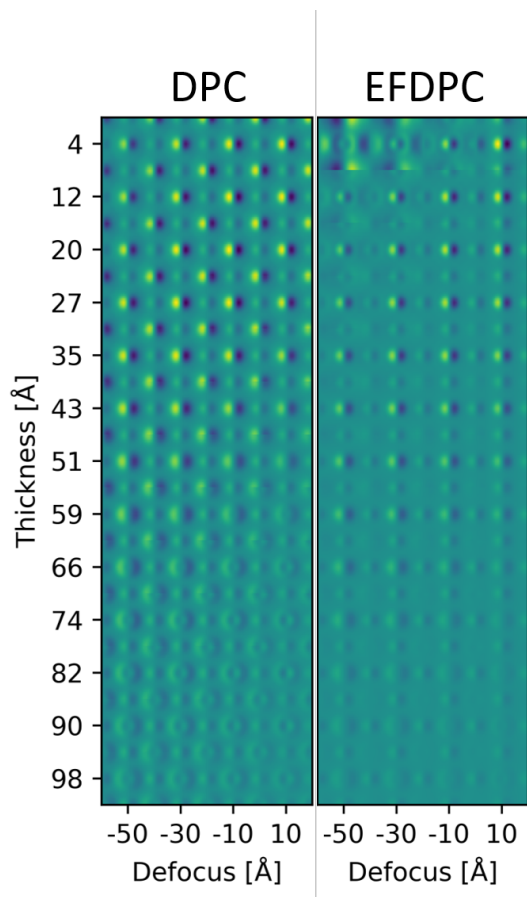


Figure 7: Thickness-defocus tableaux of SrTiO_3 elastic DPC images (left) and EFDPC 10 eV beyond the Ti L_1 -edge (right), where underfocus is negative. All images assume a 15.7 mrad probe-forming aperture and 300 keV beam energy. With elastic DPC normalized by thickness and EFDPC by the thickness squared here, the contrast within each unit cell should be independent of thickness within the phase-object approximation's domain of validity. This contrast is seen to decrease beyond about 35 Å for both regimes, evidence of the phase-object approximation starting to break down.

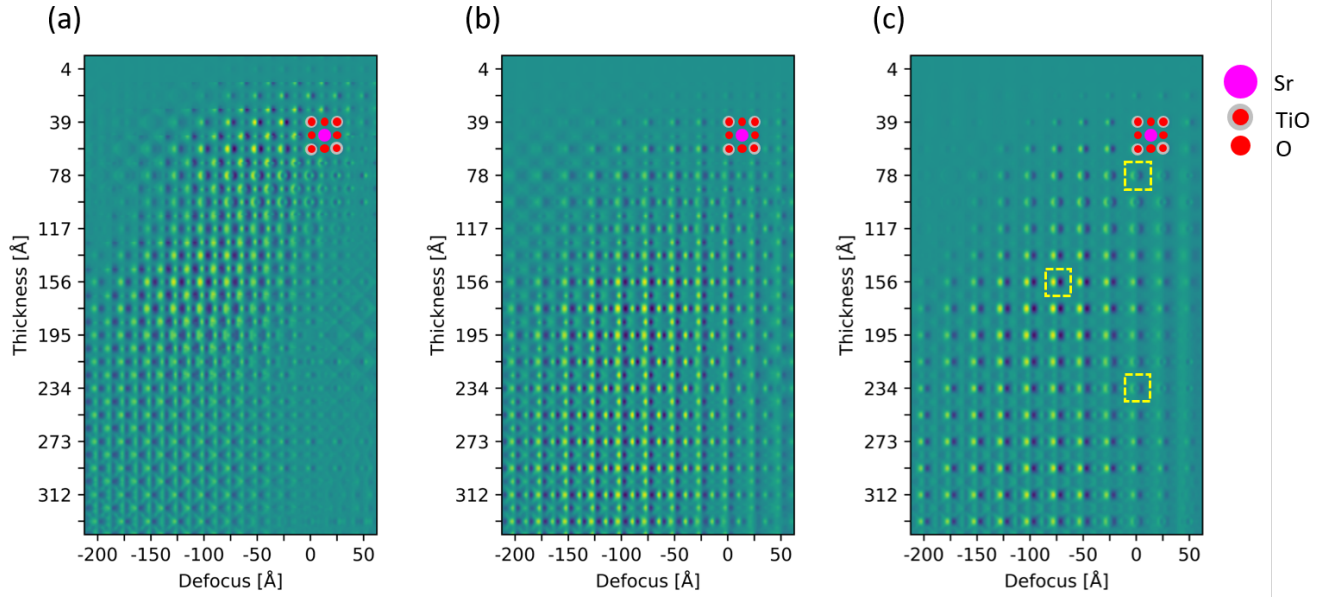


Figure 8: Thickness-defocus tableaux of SrTiO_3 for (a) elastic DPC images, (b) EFDPC images 10 eV beyond the O K-edge, and (c) EFDPC images 10 eV beyond the Ti L_1 -edge, assuming a 15.7 mrad probe-forming aperture and 300 keV beam energy, and where underfocus is negative. Elastic DPC remains interpretable for specimens of thickness of around 40 Å given the probe is focused into the mid-plane of the specimen. EFDPC remains interpretable throughout the entire range observed. The emphasised tiles in (c) correspond to the parameters used in Fig. 9.

a defocus value near the specimen midplane tends to maximise the contrast. In contrast to the elastic case, where we see that the defocus-thickness combinations over which the images show clear differential phase contrast is somewhat limited, in the inelastic case the images show clear differential phase contrast over a wide range of thickness and defocus values. Atom-selective contrast is evident, with only the Ti sites clearly visible in the Ti L_1 -edge case. In the O K-edge case, we see both the pure O and TiO columns, with the latter showing higher contrast due to the larger gradient of the elastic potential on that more-strongly-scattering TiO column. Inelastic DPC thus constitutes an interesting compromise: it contains phase-contrast-like elements through preservation of elastic contrast, but maintains interpretable contrast over a wide thickness as is more usually found in incoherent imaging (somewhat reminiscent of energy filtered TEM [33]).

However, this robust interpretability does not mean that channelling effects are absent. To see this, we decompose the incoherent sum over final states in Eq. (17) to the total contribution from unit-cell-thick layers perpendicular to the optic axis. Figure 9(a) shows this layer decomposition for the tiles in the coloured boxes in Fig. 8(c), these defocus-thickness parameter combinations — $\{t = 78 \text{ Å}, \Delta f = 0 \text{ Å}\}$, $\{t = 156 \text{ Å}, \Delta f = -75 \text{ Å}\}$, and $\{t = 234 \text{ Å}, \Delta f = 0 \text{ Å}\}$ — being diverse choices over the parameter space shown. We see that the contribution from different layers varies. The layers which show the clearest differential phase contrast are also those which contribute most to the signal, which helps explain the robustness of the total contrast, even though the contribution from some layers is far less directly interpretable. Which layers contribute the most

varies widely for the different defocus-thickness parameter combinations: in Fig. 8(b) the layers near the midplane dominate the intensity; in Fig. 8(c) the layers prior to the midplane dominate; in Fig. 8(d) the layers prior and subsequent to the mid-plane provide comparable contributions. Note too that the layers which contribute the most are not necessarily those at the nominal in-focus plane. Nevertheless, in each case the sum over layers produces a fairly similar total image, consistent with the fairly uniform contrast in Fig. 8(c).

That different depths contribute differently has been well established in inelastic STEM imaging, both in the context of high angle annular dark field imaging and electron energy loss spectroscopy [38, 39, 40, 41]. In both cases, the underlying cause is the way the probe electron wavefield evolves through the sample. The intensity distribution of an atomically fine electron probe on an atomic column oscillates with propagation along the columns, at some depths peaking up on the columns and at others spreading out. One way of visualising this is to evaluate the integrated elastically-scattered electron probe intensity within a certain radius of the column, i.e.

$$\sigma(z) = \int_{\text{disk}} d\mathbf{r}_{\perp} |\psi_0(\mathbf{r}_{\perp}, z)|^2 \quad (24)$$

(this is not conventionally a cross-section, but the reasons for this notation will become clear presently). For the probe centred on the Ti column, this is plotted as the orange line, labelled “ σ w/ top-hat”, in Fig. 8(b)-(d) for the three different thickness and defocus parameter combinations considered previously, and this integrated intensity is seen to vary with layer depth. That this behaviour largely underpins the layer dependence of the EFDPC signal can be motivated by the following series of models of increasing complexity.

The cross-section expression for electron energy loss spectroscopy is given by [40]:

$$\sigma_{\text{layer}}(z) = \int_z^{z+u_z} dz \int d\mathbf{r}_{\perp} |\psi_0(\mathbf{r}_{\perp}, z)|^2 V_{\text{eff}}(\mathbf{r}_{\perp}, z), \quad (25)$$

where u_z is the layer thickness, $V_{\text{eff}}(\mathbf{r}_{\perp}, z)$ is an effective scattering potential for the inelastic transition and incorporating the detector geometry⁷, and this model neglects elastic scattering after the inelastic scattering event. The blue dotted lines, labeled σ , in Fig. 8(b)-(d) show the Ti L_1 -edge signal calculated in this model, assuming a 35 eV energy window above threshold and a very large detector collection angle. The radius of the disk integration region used to evaluate Eq. (24) was chosen to be that containing 60% of the effective scattering potential V_{eff} since it gave the most favourable agreement with the results of Eq. (25). Nevertheless, and while not identical, the similarity in the plots supports the channelling behaviour being the primary cause of the oscillations seen.

The green lines in Fig. 8(b)-(d) were calculated using the transition potential model of Eq. (23), assuming an energy filter 10 eV above the Ti L_1 -edge and a large detector. Since this quantity is the would-be-observed intensity on an EELS spectrum at the corresponding energy loss, the signal is labelled “total EELS”. By including absorption due to thermal scattering after the ionization

⁷For notational simplicity, we have absorbed into V_{eff} the prefactors that more conventionally appear in front of Eq. (25).

event and restricting to a single energy loss, the assumptions of this calculation differ somewhat from that of the cross-section expression. (Elastic scattering after the ionization event is also included, but that redistribution will not much affect the total inelastic intensity.) Nevertheless, the total EELS signal and the cross-section expression are in close agreement, suggesting those differences have only a small effect on the depth dependence of the signal.

Since these plots considered the probe on the column site, where the EFDPC signal is zero, the blue lines in Fig. 8(b)-(d) show instead the energy-filtered iDPC (EFiDPC) signal, which is peaked on the column. The EFDPC x and y signals are not strictly partial derivatives of the same function even in the thin sample regime, Eq. (19), but the procedure on the right hand side of Eq. (21) can still be applied and, as shown in the select layer insets in Fig. 8(b)-(d), the resultant images have the expected qualitative form of an iDPC signal when the DPC signals are directly interpretable. Though the blue lines show more differences from the other lines, which we attribute largely to elastic scattering after the inelastic scattering event having some impact on the DPC value, their general shape is broadly quite similar, with clear correspondence between the peaks and troughs. This is consistent with channelling being the underlying mechanism for the variation in contributions from different layers.

5. Conclusion

In this work we have presented a theoretical interpretation and explored the imaging dynamics of energy-filtered DPC imaging, where the energy filter selects electrons that have caused inner shell ionization.

Within the phase object approximation applicable to thin samples, we have shown that the contrast is similar to that of elastic DPC imaging because the elastic DPC contrast is preserved within the momentum distribution of inelastically scattered electrons, over a spatial region corresponding to the range of appreciable ionization probability. For low energy losses and light elements, this means that the EFDPC signal at an energy loss corresponding to a particular element may include contrast from nearby atoms of different species, explaining why nitrogen atom sites are visible in the boron K-shell EFDPC experimental results of Haas and Koch [20]. However, for heavier elements the range of the ionization interaction is much narrower, and element selective DPC contrast is expected.

For thick specimens, say beyond several nanometres, the phase object approximation breaks down quantitatively for both EFDPC and elastic DPC. However, we have shown that qualitatively the EFDPC images remain interpretable to much larger thicknesses than do elastic DPC images, a consequence of the incoherence between the contributions from the different atoms. Despite this more robust appearance, we have also shown that the contribution from different depths within the sample differ as a result of the nonuniform evolution of the probe wavefield along the atomic columns.

EFDPC thus combines the advantages of STEM EELS and elastic DPC. Indeed, the strengths of each mitigate against limitations in the other. The delocalisation of EELS is mitigated by manifesting as a modulation of the gradient of the elastic potential. This may allow the position of atoms to be more precisely determined, for instance when probing orientation relationships between a thin surface layer and a substrate. Conversely, the limited thickness range of interpretable elastic

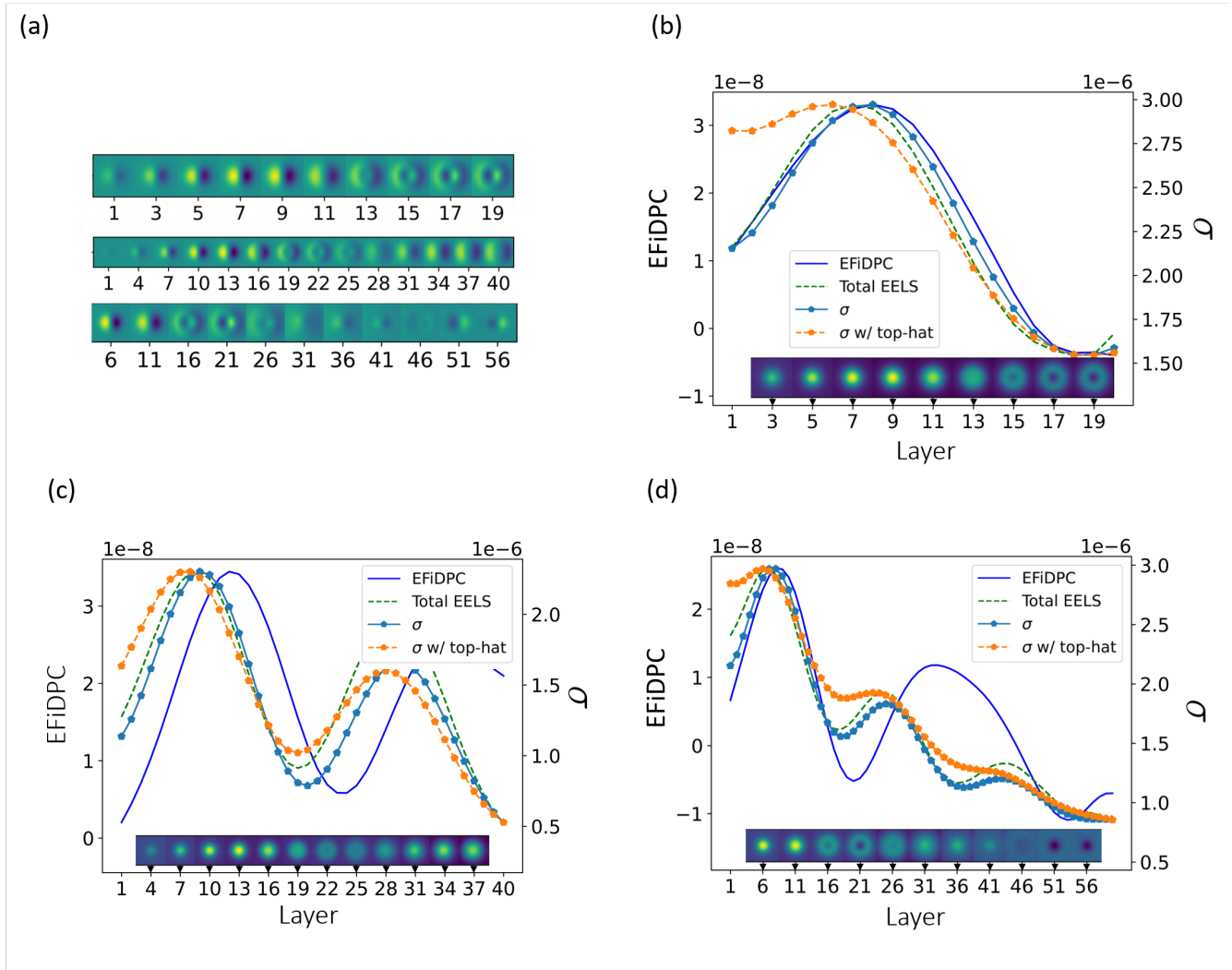


Figure 9: (a) Layer contributions (from a sub-set of layers) to the EFDPC images for the three different thickness and defocus parameter combinations indicated by the coloured boxes in Fig. 8(c), specifically 78.1 Å (20 layers) and surface defocus (top), 156.2 Å (40 layers) and -75 Å defocus (middle), and 234.3 Å (60 layers) and surface defocus (bottom), all assuming SrTiO₃ specimen, 300 keV beam electrons, 15.7 mrad aperture and energy filter placed 10 eV beyond the Ti L₁-edge. A layer is taken to be the depth of a unitcell i.e. 3.9 Å. For each of the three cases respectively, (b), (c) and (d) plot the energy-filtered, integrated DPC (EFIDPC), integrated inelastic intensity (total EELS), scattering cross-section (σ , Eq. (25)), and the scattering cross-section with a top-hat function (σ w/ top-hat, Eq. (24)) for the probe on the TiO column as a function of layer depth. Insets show the 2D EFIDPC maps about the TiO column. All plots are scaled such that maxima and minima align, with the units for the EFIDPC signal given on the left axis and those for the cross-section given on the right. The broad similarity between the plots results from the underlying channelling of the probe being common to each signal.

DPC images has been mitigated by the incoherence of EELS, making direct interpretation possible in much thicker samples, extending the range of samples over which reliable DPC-like contrast can be achieved. Further work is needed in developing procedures to acquire core-loss filtered 4D STEM data to determine whether EFDPC might be convenient and/or competitive over separately recording EELS and elastic DPC images when seeking such structural insights. Irrespective, the present results offer some initial insights into the prospects of energy-filtered 4D STEM.

CRediT authorship contribution statement

M. Deimetry: Methodology, Software, Formal analysis, Investigation, Writing - Original Draft, Writing - Review & Editing, Visualization. **T.C. Petersen:** Conceptualization, Methodology, Writing - Review & Editing, Supervision. **H.G. Brown:** Methodology, Software, Writing - Review & Editing. **M. Weyland:** Conceptualization, Methodology, Writing - Review & Editing, Supervision. **S.D. Findlay:** Conceptualization, Methodology, Validation, Writing - Review & Editing, Funding acquisition.

Declaration of competing interest

The authors declare that they have no known competing financial interests or personal relationships that could have appeared to influence the work reported in this paper.

Acknowledgments

This research is supported by an Australian Government Research Training Program Scholarship. This research was supported under the Discovery Projects funding scheme of the Australian Research Council (Project No. FT190100619).

Appendix A. Vanishing of the first moment of inelastic diffraction patterns if elastic scattering did not occur

The diffraction intensity for wavefields $\psi_0 H_{n\ell m \rightarrow \varepsilon \ell' m'}$ summed over m and m' is given by

$$\begin{aligned} \mathcal{I}(\mathbf{k}_\perp, \mathbf{R}) &= \sum_{m, m'} |(\Psi_0(\mathbf{k}_\perp) e^{-2\pi i \mathbf{k}_\perp \cdot \mathbf{R}}) \otimes H_{n\ell m \rightarrow \varepsilon \ell' m'}(\mathbf{k}_\perp)|^2 \\ &= \int d\boldsymbol{\tau} d\boldsymbol{\gamma} \Psi_0(\mathbf{k} - \boldsymbol{\tau}) \Psi_0^*(\mathbf{k} - \boldsymbol{\gamma}) e^{2\pi i (\boldsymbol{\tau} - \boldsymbol{\gamma}) \cdot \mathbf{R}} \left[\sum_{m, m'} H_{n\ell m \rightarrow \varepsilon \ell' m'}(\boldsymbol{\tau}) H_{n\ell m \rightarrow \varepsilon \ell' m'}^*(\boldsymbol{\gamma}) \right], \end{aligned} \quad (\text{A.1})$$

where \otimes denotes convolution. To evaluate the term in square brackets, let us first re-write the transition matrix element as

$$H_{n\ell m \rightarrow \varepsilon \ell' m'}(\mathbf{k}) = \frac{q_e^2}{4\pi^2 \varepsilon_0 k^2} \sum_{\ell''=0}^{\infty} \sum_{m''=-\ell''}^{\ell''} (-i)^{\ell''} Y_{\ell''}^{m''}(\hat{\mathbf{k}}) \langle l' m' | \overline{l'' m''} | l m \rangle R_{l', l'' l}(k) \quad (\text{A.2})$$

(which simplifies to Eq. (6) on using the properties of the Wigner $3j$ symbols in Eq. (7)). Anticipating that it will depend only on the magnitudes τ and γ and on the dot product $\hat{\boldsymbol{\tau}} \cdot \hat{\boldsymbol{\gamma}}$, the term in square brackets can then be written as

$$\begin{aligned}
F(\tau, \gamma, \hat{\boldsymbol{\tau}} \cdot \hat{\boldsymbol{\gamma}}) &= \sum_{m, m'} H_{n\ell m \rightarrow \varepsilon \ell' m'}(\boldsymbol{\tau}) H_{n\ell m \rightarrow \varepsilon \ell' m'}^*(\boldsymbol{\gamma}) \\
&= \frac{q_e^4}{(4\pi^2 \varepsilon_0)^2 \tau^2 \gamma^2} \sum_{\ell''=0}^{\infty} \sum_{\ell'''=0}^{\infty} \sum_{m''=-\ell''}^{\ell''} \sum_{m'''=-\ell'''}^{\ell'''} (-i)^{\ell''-\ell'''} Y_{\ell''}^{m''}(\hat{\boldsymbol{\tau}}) Y_{\ell'''}^{m'''*}(\hat{\boldsymbol{\gamma}}) R_{\nu, \ell'', \ell}(\tau) R_{\nu, \ell''', \ell}(\gamma) \\
&\quad \sum_{m, m'} \langle \ell' m' | \ell'' m'' | \ell m \rangle \langle \ell' m' | \ell''' m''' | \ell m \rangle \\
&= \frac{q_e^4}{(4\pi^2 \varepsilon_0)^2 \tau^2 \gamma^2} \frac{(2\ell' + 1)(2\ell + 1)}{4\pi} \sum_{\ell''=0}^{\infty} R_{\nu, \ell'', \ell}(\tau) R_{\nu, \ell'', \ell}(\gamma) \begin{pmatrix} \ell' & \ell'' & \ell \\ 0 & 0 & 0 \end{pmatrix}^2 \\
&\quad \sum_{m''=-\ell''}^{\ell''} Y_{\ell''}^{m''}(\hat{\boldsymbol{\tau}}) Y_{\ell''}^{m''*}(\hat{\boldsymbol{\gamma}}) \\
&= \frac{q_e^4}{(4\pi^2 \varepsilon_0)^2 \tau^2 \gamma^2} \frac{(2\ell' + 1)(2\ell + 1)}{4\pi} \sum_{\ell''=0}^{\infty} R_{\nu, \ell'', \ell}(\tau) R_{\nu, \ell'', \ell}(\gamma) \begin{pmatrix} \ell' & \ell'' & \ell \\ 0 & 0 & 0 \end{pmatrix}^2 \\
&\quad \frac{(2\ell'' + 1)}{4\pi} P_{\ell''}(\hat{\boldsymbol{\tau}} \cdot \hat{\boldsymbol{\gamma}}), \tag{A.3}
\end{aligned}$$

where the third equality follows from the orthogonality relation

$$(2j_3 + 1) \sum_{m_1, m_2} \begin{pmatrix} j_1 & j_2 & j_3 \\ m_1 & m_2 & m_3 \end{pmatrix} \begin{pmatrix} j_1 & j_2 & j_3' \\ m_1 & m_2 & m_3' \end{pmatrix} = \delta_{j_3, j_3'} \delta_{m_3, m_3'}, \tag{A.4}$$

and the fourth equality follows from the addition theorem

$$P_{\ell''}(\hat{\boldsymbol{x}} \cdot \hat{\boldsymbol{y}}) = \frac{4\pi}{2\ell'' + 1} \sum_{m''=-\ell''}^{\ell''} Y_{\ell''}^{m''}(\hat{\boldsymbol{y}}) Y_{\ell''}^{m''*}(\hat{\boldsymbol{x}}). \tag{A.5}$$

Thus we can rewrite Eq. (A.1) as

$$\mathcal{I}(\mathbf{k}_{\perp}, \mathbf{R}) = \int d\boldsymbol{\tau} d\boldsymbol{\gamma} \Psi_0(\mathbf{k} - \boldsymbol{\tau}) \Psi_0^*(\mathbf{k} - \boldsymbol{\gamma}) e^{2\pi i(\boldsymbol{\tau} - \boldsymbol{\gamma}) \cdot \mathbf{R}} F(\tau, \gamma, \hat{\boldsymbol{\tau}} \cdot \hat{\boldsymbol{\gamma}}). \tag{A.6}$$

From Eq. (A.6) we may reason as follows

$$\begin{aligned}
\mathcal{I}(-\mathbf{k}_\perp, \mathbf{R}) &= \int d\boldsymbol{\tau} d\boldsymbol{\gamma} \Psi_0^*(-\mathbf{k} - \boldsymbol{\tau}) \Psi_0(-\mathbf{k} - \boldsymbol{\gamma}) e^{2\pi i(\boldsymbol{\tau} - \boldsymbol{\gamma}) \cdot \mathbf{R}} F(\boldsymbol{\tau}, \boldsymbol{\gamma}, \hat{\boldsymbol{\tau}} \cdot \hat{\boldsymbol{\gamma}}) \\
&= \int d\boldsymbol{\tau} d\boldsymbol{\gamma} \Psi_0^*(-\mathbf{k} + \boldsymbol{\tau}) \Psi_0(-\mathbf{k} + \boldsymbol{\gamma}) e^{-2\pi i(\boldsymbol{\tau} - \boldsymbol{\gamma}) \cdot \mathbf{R}} F(\boldsymbol{\tau}, \boldsymbol{\gamma}, \hat{\boldsymbol{\tau}} \cdot \hat{\boldsymbol{\gamma}}) \\
&= \int d\boldsymbol{\tau} d\boldsymbol{\gamma} \Psi_0^*(-\mathbf{k} + \boldsymbol{\gamma}) \Psi_0(-\mathbf{k} + \boldsymbol{\tau}) e^{2\pi i(\boldsymbol{\tau} - \boldsymbol{\gamma}) \cdot \mathbf{R}} F(\boldsymbol{\gamma}, \boldsymbol{\tau}, \hat{\boldsymbol{\tau}} \cdot \hat{\boldsymbol{\gamma}}) \\
&= \int d\boldsymbol{\tau} d\boldsymbol{\gamma} \Psi_0^*(\mathbf{k} - \boldsymbol{\tau}) \Psi_0(\mathbf{k} - \boldsymbol{\gamma}) e^{2\pi i(\boldsymbol{\tau} - \boldsymbol{\gamma}) \cdot \mathbf{R}} F(\boldsymbol{\tau}, \boldsymbol{\gamma}, \hat{\boldsymbol{\tau}} \cdot \hat{\boldsymbol{\gamma}}) \\
&= \mathcal{I}(\mathbf{k}_\perp, \mathbf{R})
\end{aligned} \tag{A.7}$$

where in the second line we have made the change of variables $\boldsymbol{\tau} \rightarrow -\boldsymbol{\tau}$ and $\boldsymbol{\gamma} \rightarrow -\boldsymbol{\gamma}$, in the third line we have exchanged the dummy variables of integration, and in the fourth line we have assumed that $\Psi_0^*(-\mathbf{k}) = \Psi_0(\mathbf{k})$, which would hold for a rotationally-symmetric, aberration-free probe, and used the property of Eq. (A.3) that $F(\boldsymbol{\tau}, \boldsymbol{\gamma}, \hat{\boldsymbol{\tau}} \cdot \hat{\boldsymbol{\gamma}}) = F(\boldsymbol{\gamma}, \boldsymbol{\tau}, \hat{\boldsymbol{\tau}} \cdot \hat{\boldsymbol{\gamma}})$. Equation (A.7) shows that the inelastic diffraction pattern is inversion symmetric, and it then immediately follows that its centre of mass is zero:

$$\int d\mathbf{k}_\perp k_x \sum_{m,m'} \mathcal{I}(\mathbf{k}_\perp) = \int d\mathbf{k}_\perp (-k_x) \sum_{m,m'} \mathcal{I}(-\mathbf{k}_\perp) = - \int d\mathbf{k}_\perp k_x \sum_{m,m'} \mathcal{I}(\mathbf{k}_\perp) = 0 \tag{A.8}$$

(the same result follows for the y -direction). Hence the first moment of an inelastic diffraction pattern would be zero if elastic scattering did not occur (assuming the phase object approximation and a rotationally-symmetric, aberration-free probe).

References

- [1] K. Jarausch, P. Thomas, D. N. Leonard, R. Twesten, C. R. Booth, Four-dimensional STEM-EELS: Enabling nano-scale chemical tomography, *Ultramicroscopy* 109 (4) (2009) 326–337. doi:10.1016/j.ultramicro.2008.12.012.
- [2] C. Ophus, Four-Dimensional Scanning Transmission Electron Microscopy (4D-STEM): From Scanning Nanodiffraction to Ptychography and Beyond, *Microscopy and Microanalysis* 25 (3) (2019) 563–582. doi:10.1017/S1431927619000497.
- [3] I. MacLaren, E. Frutos-Myro, D. McGrouther, S. McFadzean, J. K. Weiss, D. Cosart, J. Portillo, A. Robins, S. Nicolopoulos, E. Nebot del Busto, et al., A comparison of a direct electron detector and a high-speed video camera for a scanning precession electron diffraction phase and orientation mapping, *Microscopy and Microanalysis* 26 (6) (2020) 1110–1116. doi:10.1017/S1431927620024411.
- [4] C. Ophus, S. E. Zeltmann, A. Bruefach, A. Rakowski, B. H. Savitzky, A. M. Minor, M. C. Scott, Automated crystal orientation mapping in py4DSTEM using sparse correlation matching, *Microscopy and microanalysis* 28 (2) (2022) 390–403. doi:10.1017/S1431927622000101.

- [5] V. Ozdol, C. Gammer, X. Jin, P. Ercius, C. Ophus, J. Ciston, A. Minor, Strain mapping at nanometer resolution using advanced nano-beam electron diffraction, *Applied Physics Letters* 106 (25) (2015). doi:10.1063/1.4922994.
- [6] C. Shi, M. C. Cao, S. M. Rehn, S.-H. Bae, J. Kim, M. R. Jones, D. A. Muller, Y. Han, Uncovering material deformations via machine learning combined with four-dimensional scanning transmission electron microscopy, *npj Computational Materials* 8 (1) (2022) 114. doi:10.1038/s41524-022-00793-9.
- [7] M. W. Tate, P. Purohit, D. Chamberlain, K. X. Nguyen, R. Hovden, C. S. Chang, P. Deb, E. Turgut, J. T. Heron, D. G. Schlom, et al., High dynamic range pixel array detector for scanning transmission electron microscopy, *Microscopy and Microanalysis* 22 (1) (2016) 237–249. doi:10.1017/S1431927615015664.
- [8] M. Krajnák, D. McGrouther, D. Maneuski, V. O’Shea, S. McVitie, Pixelated detectors and improved efficiency for magnetic imaging in stem differential phase contrast, *Ultramicroscopy* 165 (2016) 42–50. doi:10.1016/j.ultramicro.2016.03.006.
- [9] B. C. da Silva, Z. S. Momtaz, L. Bruas, J.-L. Rouvière, H. Okuno, D. Cooper, M. I. Den-Hertog, The influence of illumination conditions in the measurement of built-in electric field at p–n junctions by 4D-STEM, *Applied Physics Letters* 121 (12) (2022) 123503. doi:10.1063/5.0104861.
- [10] K. Müller, F. F. Krause, A. Béché, M. Schowalter, V. Galioit, S. Löffler, J. Verbeeck, J. Zweck, P. Schattschneider, A. Rosenauer, Atomic electric fields revealed by a quantum mechanical approach to electron picodiffraction, *Nature Communications* 5 (1) (2014) 5653. doi:10.1038/ncomms6653.
- [11] J. A. Hachtel, J. C. Idrobo, M. Chi, Sub-ångstrom electric field measurements on a universal detector in a scanning transmission electron microscope, *Advanced Structural and Chemical Imaging* 4 (2018) 1–10. doi:10.1186/s40679-018-0059-4.
- [12] H. Yang, R. Rutte, L. Jones, M. Simson, R. Sagawa, H. Ryll, M. Huth, T. Pennycook, M. Green, H. Soltau, et al., Simultaneous atomic-resolution electron ptychography and Z-contrast imaging of light and heavy elements in complex nanostructures, *Nature Communications* 7 (1) (2016) 12532. doi:10.1038/ncomms12532.
- [13] Y. Jiang, Z. Chen, Y. Han, P. Deb, H. Gao, S. Xie, P. Purohit, M. W. Tate, J. Park, S. M. Gruner, et al., Electron ptychography of 2D materials to deep sub-ångström resolution, *Nature* 559 (7714) (2018) 343–349. doi:10.1038/s41586-018-0298-5.
- [14] Z. Chen, Y. Jiang, Y.-T. Shao, M. E. Holtz, M. Odstrčil, M. Guizar-Sicairos, I. Hanke, S. Ganschow, D. G. Schlom, D. A. Muller, Electron ptychography achieves atomic-resolution limits set by lattice vibrations, *Science* 372 (6544) (2021) 826–831. doi:10.1126/science.abg2533.

- [15] K. C. Bustillo, S. E. Zeltmann, M. Chen, J. Donohue, J. Ciston, C. Ophus, A. M. Minor, 4D-STEM of beam-sensitive materials, *Accounts of Chemical Research* 54 (11) (2021) 2543–2551. doi:10.1021/acs.accounts.1c00073.
- [16] S. Muto, M. Ohtsuka, High-precision quantitative atomic-site-analysis of functional dopants in crystalline materials by electron-channelling-enhanced microanalysis, *Progress in Crystal Growth and Characterization of Materials* 63 (2) (2017) 40–61. doi:10.1016/j.pcrysgrow.2017.02.001.
- [17] P. Midgley, M. Saunders, R. Vincent, J. Steeds, Energy-filtered convergent-beam diffraction: examples and future prospects, *Ultramicroscopy* 59 (1-4) (1995) 1–13. doi:10.1016/0304-3991(95)00014-R.
- [18] F. Hage, T. Hardcastle, A. Scott, R. Brydson, Q. Ramasse, Momentum- and space-resolved high-resolution electron energy loss spectroscopy of individual single-wall carbon nanotubes, *Physical Review B* 95 (19) (2017) 195411. doi:10.1103/PhysRevB.95.195411.
- [19] R. Qi, N. Li, J. Du, R. Shi, Y. Huang, X. Yang, L. Liu, Z. Xu, Q. Dai, D. Yu, et al., Four-dimensional vibrational spectroscopy for nanoscale mapping of phonon dispersion in BN nanotubes, *Nature Communications* 12 (1) (2021) 1179. doi:10.1038/s41467-021-21452-5.
- [20] B. Haas, C. T. Koch, Momentum- and Energy-Resolved STEM at Atomic Resolution, *Microscopy and Microanalysis* 28 (S1) (2022) 406–408. doi:10.1017/S1431927622002343.
- [21] C. Dwyer, Multislice theory of fast electron scattering incorporating atomic inner-shell ionization, *Ultramicroscopy* 104 (2) (2005) 141–151. doi:10.1016/j.ultramicro.2005.03.005.
- [22] C. Dwyer, S. D. Findlay, L. J. Allen, Multiple elastic scattering of core-loss electrons in atomic resolution imaging, *Physical Review B* 77 (18) (2008) 184107. doi:10.1103/PhysRevB.77.184107.
- [23] H. G. Brown, J. Ciston, C. Ophus, Linear-scaling algorithm for rapid computation of inelastic transitions in the presence of multiple electron scattering, *Physical Review Research* 1 (3) (2019) 033186, publisher: American Physical Society. doi:10.1103/PhysRevResearch.1.033186.
- [24] K. Müller-Caspary, F. F. Krause, T. Grieb, S. Löffler, M. Schowalter, A. Béché, V. Galioit, D. Marquardt, J. Zweck, P. Schattschneider, et al., Measurement of atomic electric fields and charge densities from average momentum transfers using scanning transmission electron microscopy, *Ultramicroscopy* 178 (2017) 62–80. doi:10.1016/j.ultramicro.2016.05.004.
- [25] A. J. D’Alfonso, E. C. Cosgriff, S. D. Findlay, G. Behan, A. I. Kirkland, P. D. Nellist, L. J. Allen, Three-dimensional imaging in double aberration-corrected scanning confocal electron microscopy, Part II: Inelastic scattering, *Ultramicroscopy* 108 (12) (2008) 1567–1578. doi:10.1016/j.ultramicro.2008.05.007.

- [26] W. Coene, D. Van Dyck, Inelastic scattering of high-energy electrons in real space, *Ultramicroscopy* 33 (4) (1990) 261–267. doi:10.1016/0304-3991(90)90043-L.
- [27] X. Wang, P. Li, M. Malac, R. Lockwood, A. Meldrum, The spatial distribution of silicon NCs and erbium ion clusters by simultaneous high-resolution energy filtered and Z-contrast STEM and transmission electron tomography, *Physica Status Solidi C* 8 (3) (2011) 1038–1043. doi:10.1002/pssc.201000393.
- [28] H. L. Xin, C. Dwyer, D. A. Muller, Is there a Stobbs factor in atomic-resolution STEM-EELS mapping?, *Ultramicroscopy* 139 (2014) 38–46. doi:10.1016/j.ultramic.2014.01.006.
- [29] M. Oxley, L. Allen, Atomic scattering factors for K-shell and L-shell ionization by fast electrons, *Acta Crystallographica Section A: Foundations of Crystallography* 56 (5) (2000) 470–490. doi:10.1107/s0108767300007078.
- [30] H. Brown, `py_multislice`, https://github.com/HamishGBrown/py_multislice.
- [31] I. Lazić, E. G. T. Bosch, S. Lazar, Phase contrast STEM for thin samples: Integrated differential phase contrast, *Ultramicroscopy* 160 (2016) 265–280. doi:10.1016/j.ultramic.2015.10.011.
- [32] A. Howie, Inelastic scattering of electrons by crystals. I. the theory of small-angle in elastic scattering, *Proceedings of the Royal Society of London. Series A. Mathematical and Physical Sciences* 271 (1345) (1963) 268–287. doi:10.1098/rspa.1963.0017.
- [33] H. Brown, A. D’Alfonso, B. Forbes, L. Allen, Addressing preservation of elastic contrast in energy-filtered transmission electron microscopy, *Ultramicroscopy* 160 (2016) 90–97. doi:10.1016/j.ultramic.2015.10.001.
- [34] C. Kottler, C. David, F. Pfeiffer, O. Bunk, A two-directional approach for grating based differential phase contrast imaging using hard x-rays, *Opt. Express* 15 (3) (2007) 1175–1181. doi:10.1364/OE.15.001175.
- [35] A. Beyer, F. F. Krause, H. L. Robert, S. Firoozabadi, T. Grieb, P. Kükkelhan, D. Heimes, M. Schowalter, K. Müller-Caspary, A. Rosenauer, et al., Influence of plasmon excitations on atomic-resolution quantitative 4D scanning transmission electron microscopy, *Scientific reports* 10 (1) (2020) 17890. doi:10.1038/s41598-020-74434-w.
- [36] R. Close, Z. Chen, N. Shibata, S. D. Findlay, Towards quantitative, atomic-resolution reconstruction of the electrostatic potential via differential phase contrast using electrons, *Ultramicroscopy* 159 (2015) 124–137. doi:10.1016/j.ultramic.2015.09.002.
- [37] F. Winkler, J. Barthel, R. E. Dunin-Borkowski, K. Müller-Caspary, Direct measurement of electrostatic potentials at the atomic scale: A conceptual comparison between electron holography and scanning transmission electron microscopy, *Ultramicroscopy* 210 (2020) 112926. doi:10.1016/j.ultramic.2019.112926.

- [38] S. Hillyard, R. F. Loane, J. Silcox, Annular dark-field imaging: resolution and thickness effects, *Ultramicroscopy* 49 (1-4) (1993) 14–25. doi:10.1016/0304-3991(93)90209-G.
- [39] C. Dwyer, J. Etheridge, Scattering of Å-scale electron probes in silicon, *Ultramicroscopy* 96 (3-4) (2003) 343–360. doi:10.1016/S0304-3991(03)00100-1.
- [40] L. Allen, S. Findlay, M. Oxley, C. Rossouw, Lattice-resolution contrast from a focused coherent electron probe. Part I, *Ultramicroscopy* 96 (1) (2003) 47–63. doi:10.1016/S0304-3991(02)00380-7.
- [41] P. Voyles, D. Muller, E. Kirkland, Depth-dependent imaging of individual dopant atoms in silicon, *Microscopy and Microanalysis* 10 (2) (2004) 291–300. doi:0.1017/S1431927604040012.

Supplementary Material for “Differential phase contrast from electrons that cause inner shell ionization”

Michael Deimetry^a, Timothy C. Petersen^b, Hamish G. Brown^c, Matthew Weyland^b,
Scott D. Findlay^{a,*}

^a*School of Physics and Astronomy, Monash University, Clayton, Victoria, 3800, Australia*

^b*Monash Centre for Electron Microscopy, Monash University, Clayton, Victoria, 3800, Australia*

^c*Ian Holmes Imaging Center, University of Melbourne, Parkville, Victoria, 3052, Australia*

1. Derivation of Eq. (11)

To evaluate Eq. (10), we use Parseval’s theorem,

$$\int_{-\infty}^{\infty} d\mathbf{r}_{\perp} |H_{fi}(\mathbf{r}_{\perp})|^2 = \int_{-\infty}^{\infty} d\mathbf{k}_{\perp} |H_{fi}(\mathbf{k}_{\perp})|^2, \quad (1)$$

and set $\boldsymbol{\tau} = \boldsymbol{\gamma} = \mathbf{k}_{\perp}$ in (A.3) to give

$$\begin{aligned} T_{\ell'}(n\ell, \varepsilon) &= \int d\mathbf{k}_{\perp} \sum_{m,m'} |H_{n\ell m \rightarrow \varepsilon \ell' m'}(\mathbf{k}_{\perp})|^2 \\ &= \frac{q_e^4}{(4\pi^2 \varepsilon_0)^2} \frac{(2\ell' + 1)(2\ell + 1)}{(4\pi)^2} \sum_{\ell''=0}^{\infty} \begin{pmatrix} \ell' & \ell'' & \ell \\ 0 & 0 & 0 \end{pmatrix}^2 (2\ell'' + 1) \int \frac{d\mathbf{k}_{\perp}}{k^4} R_{\nu, \nu', l}(k)^2 \end{aligned} \quad (2)$$

where we have used the fact that $P_{\ell'}(\hat{\mathbf{k}} \cdot \hat{\mathbf{k}}) = 1$. We focus on the weighted radial wave function overlap integral $R_{\nu, \nu', l}(k)$ in Eq. (8), reproduced here for convenience:

$$R_{\nu, \nu', l}(k) = \int_0^{\infty} dr P_{\varepsilon \ell'}(r) j_{\ell''}(kr) P_{n\ell}(r). \quad (3)$$

To proceed with this integral we need to obtain expressions for the bound and continuum radial wave functions.

An analytic form for the bound wave function can be obtained using variational methods [42]. The form chosen is given by the Slater-type orbital

$$P_{n^* \ell}(r) = N r^{n^*} e^{-\zeta r}, \quad (4)$$

*Corresponding author

Email address: `scott.findlay@monash.edu` (Scott D. Findlay)

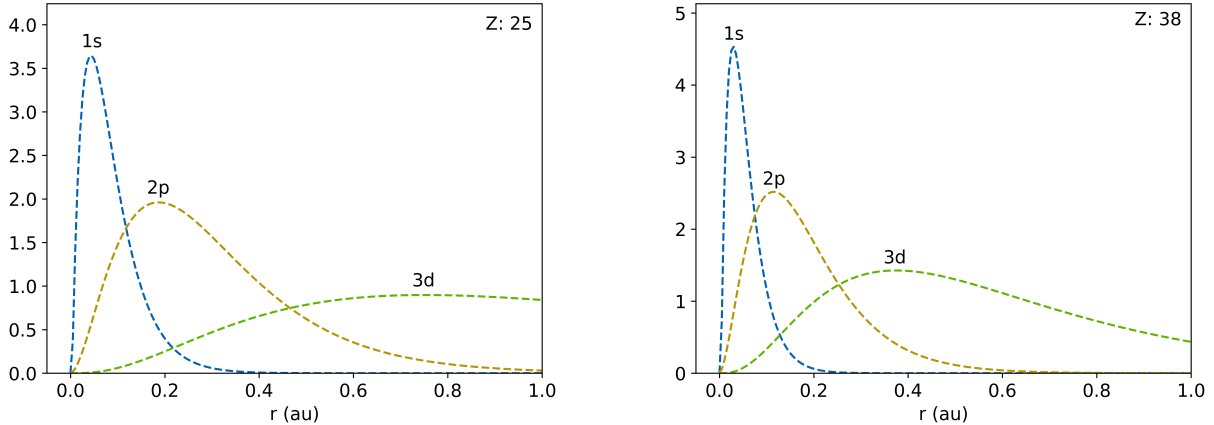


Figure 1: Bound radial wave functions for various quantum numbers.

where $N = (2\zeta)^{n^*} (2\zeta/\Gamma(2n^* + 1))^{1/2}$ is the normalization, r is the distance from the nucleus in atomic units and $\zeta = (Z - s)/n^*$ where Z is the atomic number, n^* is a modified principal quantum number (which equals n if $n \leq 3$) and s is a so-called shielding factor. The remainder of this argument will only follow for bound states which are nodeless with non-negative range, for instance, $1s$, $2p$ or $3d$. These are illustrated in Fig. 1, where it is seen that they are only non-zero in close vicinity of the origin, consistent with the decaying exponential term in Eq. (4).

The unbound radial wave functions, $P_{\varepsilon\ell'}$, satisfy the differential equation [43]

$$\left[-\frac{d^2}{dr^2} + \frac{\ell'(\ell' + 1)}{r^2} + V_{\varepsilon\ell'}(r) \right] P_{\varepsilon\ell'}(r) = \varepsilon P_{\varepsilon\ell'}(r). \quad (5)$$

Here $V_{\varepsilon\ell'}$ is the radial potential of the atom after an electron has been ejected with energy ε above the ionization threshold given now in Rydberg units to reduce notational clutter. Since the radial norm of $P_{\varepsilon\ell'}(r)$ is not finite, we adopt the normalization convention [43]

$$\int_0^\infty P_{\varepsilon\ell'}(r) P_{\varepsilon'\ell'}(r) dr = \delta(\varepsilon - \varepsilon'). \quad (6)$$

Since the bound state wavefunctions are localised near the origin in r , as seen in Fig. 1, for the purpose of evaluating $R_{\ell',\nu',\nu}(k)$ in Eq. (3) we are primarily interested in the form of $P_{\varepsilon\ell'}(r)$ for small r . In this regime, if ℓ' is sufficiently large the centrifugal barrier term $\frac{\ell'(\ell'+1)}{r^2}$ will dominate over the potential term $V_{\varepsilon\ell'}(r)$ and we can approximate Eq. (5) to

$$\left[-\frac{d^2}{dr^2} + \frac{\ell'(\ell' + 1)}{r^2} \right] P_{\varepsilon\ell'}(r) = \varepsilon P_{\varepsilon\ell'}(r), \quad (7)$$

which has general solution

$$P_{\varepsilon\ell'}(r) \approx \sqrt{r} J_\nu(r\sqrt{\varepsilon}) c_1 + \sqrt{r} Y_\nu(r\sqrt{\varepsilon}) c_2, \quad (8)$$

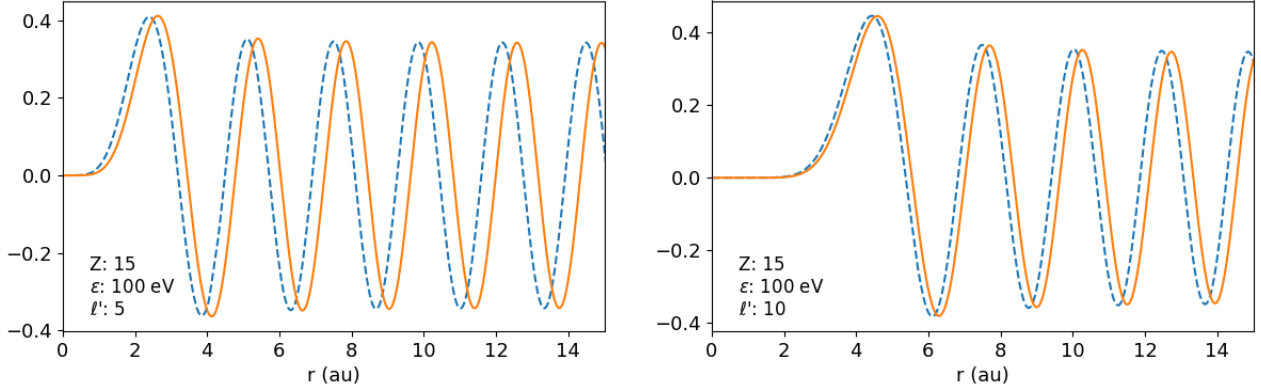


Figure 2: Continuum wave function obtained by solving Eq. (5) (dotted) in comparison with Eq. (10) (solid) which neglects the potential. For large ℓ' the centrifugal barrier dominates. This result is weakly dependent on Z and ε .

where J and Y denote Bessel functions of the first and second kinds respectively, the subscript denotes the order and c denote arbitrary constants. To satisfy the boundary condition

$$P_{\varepsilon\ell'}(r) \rightarrow 0 \quad \text{as } r \rightarrow 0 \quad (9)$$

it follows that

$$P_{\varepsilon\ell'}(r) \approx c\sqrt{r}J_{\ell'+1/2}(r\sqrt{\varepsilon}) . \quad (10)$$

Using the large x asymptotic result that [44]

$$J_{\nu}(x) \sim \sqrt{\frac{2}{\pi x}} \cos(x - \delta_{\nu}) , \quad (11)$$

it can be shown that the choice $c = 1/\sqrt{2}$ satisfies the normalisation condition of Eq. (6).

Some examples of the approximate continuum radial wave function $P_{\varepsilon\ell'}(r)$ in Eq. (10) in comparison with the true solution are illustrated in Fig. 2. As expected, increasing the centrifugal barrier by increasing ℓ' reduces the relative effect of the atom potential, bringing the approximate solution closer to the exact solution.

Being interested in the small r regime, we simplify the radial wave functions integral further using the asymptotic approximation [44]

$$J_{\nu}(r) \sim \frac{e^{\nu - (\nu + \frac{1}{2}) \log(\nu) + \nu \log(r/2)}}{\sqrt{2\pi}} + \mathcal{O}(1/\nu) , \quad (12)$$

to yield

$$P_{\varepsilon\ell'}(r) \approx \sqrt{\frac{r}{2}} \frac{e^{\nu - (\nu + \frac{1}{2}) \log(\nu) + \nu \log(r\sqrt{\varepsilon}/2)}}{\sqrt{2\pi}} . \quad (13)$$

where $\nu = \ell' + 1/2$. Although we have analytic forms for all the factors in the integrand in Eq. (3), the resultant integral still does not admit an analytic solution. We therefore make further approximations. We begin by applying the Cauchy-Schwarz inequality to obtain

$$|R(k)|^2 = \left| \int_0^\infty dr P_{\varepsilon\ell'}(r) j_{\ell''}(kr) P_{n^*\ell}(r) \right|^2 \leq \int_0^\infty dr |P_{\varepsilon\ell'}(r) P_{n^*\ell}(r)|^2 \int_0^\infty dr j_{\ell''}(kr)^2 \text{ for } k > 0, \quad (14)$$

which is a crude bound but, as we will see, is sufficient to imply an exponential fall-off.

Substituting Eq. (4) and Eq. (13) into the first integral on the right in Eq. (14) gives

$$\int_0^\infty dr |P_{\varepsilon\ell'}(r) P_{n^*\ell}(r)|^2 = \frac{N^2}{\pi} \frac{e^{2\ell'+1} \varepsilon^{\ell'+\frac{1}{2}} \Gamma(2\ell' + 2n^* + 3)}{(2\ell' + 1)^{2(\ell'+1)} 2^{2(\ell'+n^*+2)} \zeta^{2\ell'+2n^*+3}} \quad (15)$$

The integral of the spherical Bessel function in Eq. (14) is straightforward and evaluates to

$$\int_0^\infty dr j_{\ell''}(kr)^2 = \frac{\pi}{2k(2\ell'' + 1)} \text{ if } k > 0. \quad (16)$$

Combining Eq. (14) with Eq. (2), we obtain

$$T_{\ell'}(n\ell, \varepsilon) \lesssim \frac{N^2 \pi}{12} \frac{q_e^4}{(4\pi^2 \varepsilon_0)^2} \frac{(2\ell' + 1)(2\ell + 1)}{(4\pi)^2} \sum_{\ell''} \binom{\ell' \quad \ell'' \quad \ell}{0 \quad 0 \quad 0}^2 \frac{e^{2\ell'+1} \varepsilon^{\ell'+\frac{1}{2}} \Gamma(2\ell' + 2n^* + 3)}{k_z^3 (2\ell' + 1)^{2(\ell'+1)} 2^{2(\ell'+n^*+2)} \zeta^{2\ell'+2n^*+3}}. \quad (17)$$

Taking the ratio of this with the $\ell' = 0$ term and then taking the logarithm gives

$$\log_{10} \left[\frac{T_{\ell'}(n\ell, \varepsilon)}{T_0(n\ell, \varepsilon)} \right] \approx 2\ell' \log_{10}(e/2) + \log_{10} \left(\frac{\Gamma(2\ell' + 2n^* + 3)}{(1 + 2\ell')^{1+2\ell'}} \sum_{\ell''} \binom{\ell' \quad \ell'' \quad \ell}{0 \quad 0 \quad 0}^2 \right) + \ell' \log_{10} \varepsilon - 2\ell' \log_{10}(\zeta) + \text{other terms}. \quad (18)$$

We reiterate ε in this equation is in Rydbergs while it is in electron volts in the main manuscript. This result elucidates the ε and Z dependence observed in n Fig. 4. The first terms on the right hand side of Eq. (18) dictate the rate at which the fall-off occurs. We indeed see increasing ε slows down the fall-off (by increasing or decreasing the gradient of the approximately linear behaviour in ℓ') while the converse is true for Z . This is made clearer when the relevant terms are grouped as follows:

$$\text{gradient} \approx 2 \left[\log_{10} e + \frac{1}{2} \log_{10} \varepsilon - \log_{10}(\zeta) \right] \quad (19)$$

The second term on the right in Eq. (18) is inconsequential to this main result since it only creates minor deviations from the otherwise linear dependence on ℓ' in the logarithmic form of Eq. (18),

i.e. the sequence $T_{\ell'}(n\ell, \varepsilon)$ decreases exponentially with ℓ' . The absence of k_z is in line with expectations obtained from numerical simulations since the dependence is expected to be very weak. The approximations made here have produced an expression which has entirely neglected it.

We finally note that substituting $\varepsilon \rightarrow |\varepsilon - V_0|$ can better approximate the continuum wave function near the origin where the bound wave function admits a majority of its support. Through empirical considerations, a value of $V_0 = Z^{2/7}$ has been found to work well.